PHYSICAL REVIEW B **112**, 155104 (2025)

Efficient plane-wave approach to generalized Kohn-Sham density functional theory of solids with mixed deterministic and stochastic exchange

Tucker Allen, Barry Y. Li, Tim Duong, Kajsa Williams, and Daniel Neuhauser[*]
Department of Chemistry and Biochemistry, University of California, Los Angeles, California 90095, USA

(Received 11 March 2025; revised 4 September 2025; accepted 8 September 2025; published 1 October 2025)

An efficient mixed deterministic and sparse-stochastic plane-wave approach is developed for periodic generalized-Kohn-Sham density functional theory band-structure calculations with extensive k-point sampling, for any hybrid-exchange density functional. The method works for very large elementary cells over many k points, and we benchmark it on covalently bonded solids and molecular crystals with nonbonded interactions, for systems of up to 33 000 atoms. Memory and CPU requirements scale quasilinearly with the number of atoms.

DOI: 10.1103/kr5c-csnv

I. INTRODUCTION

Generalized Kohn-Sham density functional theory (GKS-DFT), i.e., DFT with hybrid exchange-correlation (XC) functionals that include exact exchange, is now a cornerstone of electronic structure methods as such functionals reduce the self-interaction error of local and semilocal DFT for both solids and molecules [1–3]. These functionals, particularly screened hybrids that separate short- and long-range exchange [4], capture the fundamental physics in both classes of systems [5–7]. Tuned hybrids control the balance between short- and long-range exchange through a range-separation parameter γ, which is commonly obtained through either empirical fitting or first-principles calculation, e.g., by enforcing Koopmans' theorem [8]. For solids, short-range screened hybrids such as the Heyd-Scuseria-Ernzerhof (HSE06) hybrid functional produce lattice constants in good agreement with experiment for both semiconductors and insulators, while also yielding reliable band gaps for semiconductors [9–12]. Another commonly used functional, the Perdew-Burke-Ernzerhof (PBE0) global hybrid, uses a fixed fraction of exact exchange chosen based on perturbation theory arguments [13,14]. For molecules, long-range corrected (LC) hybrids enable proper description of charge-transfer and excitonic effects [4,15]. Additionally, dielectric-dependent hybrids have been successfully applied [16–21].

Exact exchange scales usually quadratically with the number of k points N_k. Many approaches have been developed to reduce the cost of evaluating exact exchange in both finite and extended systems [22–28]. However, efficient treatment of global and long-range hybrids that include a $G = 0$ singular part of the exchange kernel remains a challenge as a larger k-point mesh is required to converge observables to the thermodynamic limit.

In this article, we develop an efficient reciprocal-space plane-wave (PW) implementation of GKS-DFT. A cheap and accurate construction of the k-dependent exchange matrix is achieved for both small and very large unit cells. We introduce a general fitting procedure that uses the (semi)local-DFT wave functions sampled at the Brillouin zone center ($k = 0$, the Γ point) as a basis for the true k-dependent molecular orbitals (MOs) required for evaluating exact exchange. Then, to enable GKS-DFT calculations with dense k-point sampling we implement a mixed deterministic and sparse-stochastic approach, splitting the exchange kernel into low- and high-momentum components [29].

The starting point is a GKS-Hamiltonian

$$H = K + V_{eN} + v_H + X + v_{\mathrm{xc}}, \tag{1}$$

with the usual kinetic, nuclear, and Hartree terms; X is the Fock operator under a general explicit exchange kernel v,

$$X(r, r') = -\rho(r, r')v(r - r'), \tag{2}$$

and $v_{\mathrm{xc}}(r)$ is a (semi)local-DFT XC potential for a short-ranged kernel $|r - r'|^{-1} - v(r - r')$. The explicit exchange kernel is usually made from short- and long-range parts [1,4],

$$v(r - r') = \frac{\alpha + \beta\,\mathrm{erf}(\gamma|r - r'|)}{|r - r'|}. \tag{3}$$

The fraction of explicit exchange employed is dictated by the α and β parameters, where at small interelectronic distances, i.e., $r \to r'$, $v(r - r') = \alpha|r - r'|^{-1}$, and at large distances, i.e., $|r - r'| \to \infty$, $v(r - r') = (\alpha + \beta)|r - r'|^{-1}$. Most standard hybrid functionals are available by appropriate combinations of the α, β, and γ parameters. Various functionals are used here, including global Becke-type and range-separated hybrids that employ Fock exchange at short range, long range, or a mixture of both (see Table I).

The sampling approach of the present work exploits the differing numerical weights of the long-range (low-G) and short-range (high-G) components of the overall Coulomb kernel, $|r - r'|^{-1}$. This is illustrated for the explicit exchange, Eq. (3), by working in Fourier space,

$$v(G) = \frac{4\pi}{G^2}(\alpha + \beta e^{-G^2/4\gamma^2}), \tag{4}$$

---

[*] Contact author: dxn@ucla.edu

TABLE I. Hybrid exchange parameters per Eq. (3).

Functional	α	β	γ (bohr^{-1})
BNL	0	1	0.11
CL (CAM-LDA0)	0.19	0.46	0.33
HSE06	0.25	−0.25	0.11
PBE0	0.25	0	0

where G denotes a reciprocal lattice vector. The long-wavelength, low-G contributions carry a large numerical weight and should be treated exactly, while the high-G parts can become quite small and are amenable to data compression techniques.

II. THEORY

The periodic near-gap formalism starts analogously to the nonperiodic approach described in Refs. [29,30]. Here, lowercase functions and coordinates refer to the supercells, and uppercase ones are used within a single unit (elementary) cell. The initial step is a cheap local density approximation (LDA) (or a general DFT for local or semilocal functional) calculation for periodic systems on a supercell with N_k unit cells, which yields k-space zero-order periodic MOs, labeled $|\Phi_{pk}\rangle$.

The global Bloch states, $\phi_{nk}(r) = \frac{1}{\sqrt{N_k}} e^{ikr}\Phi_{nk}(r)$, are orthogonal on the supercell:

$$\langle\phi_{nk}|\phi_{n'k'}\rangle \equiv \int_{\text{supercell}} \phi^*_{nk}(r)\phi_{n'k'}(r)dr = \delta_{kk'}\delta_{nn'}. \tag{5}$$

For the same k, the periodic part of the Bloch states is expanded in terms of plane waves, $\Phi_{nk}(R) = \sum_G \Phi_{nk}(G)e^{iGR}$. These uppercase functions are orthogonal within a single unit cell,

$$\langle\Phi_{nk}|\Phi_{n'k}\rangle \equiv \int_{\text{elem. cell}} \Phi^*_{nk}(R)\Phi_{n'k}(R)dR = \delta_{nn'}. \tag{6}$$

A “band” of active orbitals near the Fermi level is then taken, and labeled as “near-gap” states. Specifically, for each k point we divide the states into several types: N_{core} (lower valence) states [which are of course above the inner-core states that are part of the norm-conserving pseudopotential (NCPP)]; $N_v = N_{\text{occ}} - N_{\text{core}}$ upper valence; and N_c low-lying conduction states.

The $M \equiv N_v + N_c$ near-gap orbitals are labeled as the MO-active space. Further, we introduce a subspace $A \subseteq M$, with $A \equiv A_v + A_c$, and $A_v(\leqslant N_v)$ and $A_c(\leqslant N_c)$ valence and conduction MOs, for which exchange is calculated explicitly. A is labeled as the exchange-active space. The effect of the core states on the exchange is approximated as a perturbative scissor correction, discussed later.

The GKS eigenstates on the supercell are then expanded in terms of zero-order MOs from the same k point,

$$|\psi_{ik}\rangle = \sum_j C^k_{ji}|\phi_{jk}\rangle, \tag{7}$$

where most integer indices extend over the M active orbitals, with a similar $|\Psi_{ik}\rangle = \sum_j C^k_{ji}|\Phi_{jk}\rangle$ relation for a single unit cell.

For each k, C^k is an eigenvector matrix of the k-dependent Hamiltonian matrix,

$$H^k_{jl} \equiv \langle\phi_{jk}|H|\phi_{lk}\rangle \equiv h^k_{jl} + X^k_{jl}, \tag{8}$$

where, as usual,

$$h^k_{jl} = \langle\Phi_{jk}|\frac{(k+\hat{G})^2}{2} + V_{eN} + v_H + v_{\text{xc}}|\Phi_{lk}\rangle. \tag{9}$$

Further,

$$X(r,r') = -\sum_{m\bar{k}} f_{m\bar{k}}\psi_{m\bar{k}}(r)v(r-r')\psi^*_{m\bar{k}}(r'), \tag{10}$$

where the orbital occupations are introduced. The exchange matrix elements are then in real space,

$$X^k_{jl} = \langle\phi_{jk}|X|\phi_{lk}\rangle = -\sum_{m\bar{k}} f_{m\bar{k}} \iint drdr' \times \phi^*_{jk}(r)\psi_{m\bar{k}}(r)v(r-r')\psi^*_{m\bar{k}}(r')\phi_{lk}(r'), \tag{11}$$

where the volume integrals extend over the supercell.

For the purpose of the exchange matrix elements only, we expand the k-dependent elementary functions in terms of the Γ-point functions (see also Ref. [31])

$$|\Phi_{jk}\rangle \simeq \sum_{j'} B^k_{j'j}|\Phi_{j'}\rangle, \tag{12}$$

where $B^k_{j'j} = \langle\phi_{j'}|\phi_{jk}\rangle$ and $|\Phi_{j'}\rangle \equiv |\Phi_{j',k=0}\rangle$. Note that not all ϕ_{jk} can be described properly, so for those that cannot be properly accounted for, i.e., those outside the exchange-active region, we write $B^k_{j'j} = \delta_{j'j}$. See Supplemental Material (SM) [32] for further details on the basis-set expansion.

Thus, when used in the exchange part,

$$|\Psi_{jk}\rangle \simeq \sum_{j'} D^k_{j'j}|\Phi_{j'}\rangle, \tag{13}$$

where $D^k = C^k B^k$. Thus, $X^k = (B^k)^\dagger Y^k B^k$, where the matrix element of Y^k is

$$Y^k_{jl} = -\frac{1}{N_k^2}\sum_{m\bar{k}m'm''} f_{mk}D^{\bar{k}}_{mm'}D^{\bar{k},*}_{mm''}\iint drdr' \times \Phi_j(r)\Phi_{m'}(r)e^{-i(k-\bar{k})(r-r')}v(r-r')\Phi_{m''}(r')\Phi_l(r'), \tag{14}$$

where the Γ-point wave functions are real valued. Upon Fourier transform, the exchange matrix in the reciprocal space reads

$$Y^k_{jl} = -\frac{1}{V_s}\sum_{m\bar{k}m'm''} f_{mk}D^{\bar{k}}_{mm'}D^{\bar{k},*}_{mm''} \times \sum_G \langle\Phi_j\Phi_{m'}|G\rangle v(G+k-\bar{k})\langle G|\Phi_{m''}\Phi_l\rangle, \tag{15}$$

where V_s is the supercell volume. The momentum-space representation is readily shown to be

$$Y^k_{jl} = -\sum_{i\bar{k}G} z^*_{jGi\bar{k}}z_{lGi\bar{k}}v(G+k-\bar{k}), \tag{16}$$

with rotated pair densities

$$z_{lGi\bar{k}} = \sqrt{\frac{f_{i\bar{k}}}{V_s}} \sum_t \langle G|\Phi_l \Phi_t\rangle D^{\bar{k},*}_{ti}, \tag{17}$$

and projections

$$\langle G|\Phi_l \Phi_t\rangle \equiv \int_{\text{elem. cell}} \Phi_l(R)\Phi_t(R)e^{-iGR}dR, \tag{18}$$

and the exchange kernel is

$$v(G+k-\bar{k}) \equiv \int_{\text{supercell}} v(r)e^{-i(G+k-\bar{k})r}dr. \tag{19}$$

For $G \rightarrow 0$, v in Eq.(19) could be singular, so we use a variant of the well-known Brillouin-supercell averaging [33,34]. For small arguments, we replace $v(G+k-\bar{k})$ with a modified potential:

$$\bar{v}(G+k-\bar{k}) = \frac{\int \theta_b(p)v(G+k-\bar{k}+p)dp}{\int \theta_b(p)dp}, \tag{20}$$

where $\theta_b(p)$ is the Brillouin θ function, for an orthorhombic lattice with a cell size of $L_x \cdot L_y \cdot L_z$:

$$\theta_b(p) = \theta\left(\frac{\pi}{L_x} - |p_x|\right)\theta\left(\frac{\pi}{L_y} - |p_y|\right)\theta\left(\frac{\pi}{L_z} - |p_z|\right). \tag{21}$$

The integral is obtained via a Monte Carlo procedure, for smaller $|G+k-\bar{k}|$, more sampling points are used. For all simulations, 2 million Monte Carlo points are used, and we could easily use more points to reduce the stochastic error further.

Next, we split the summation over reciprocal lattice vectors to two parts, low and high: $Y^k_{pq} = Y^{L,k}_{pq} + Y^{H,k}_{pq}$. The numerical parameter separating low from high momenta, labeled G_0, is later varied to ensure convergence. For low G, the summation is evaluated by explicitly applying Eq. (16) with $|G| < G_0$. For high $|G|$, we approximate

$$v(G+k-\bar{k}) \simeq v(G), \quad |G| > G_0. \tag{22}$$

Then $Y^{H,k}_{jl} \simeq Y^H_{jl}$, i.e., independent of wave vector k. This can be written as

$$Y^H_{jl} \simeq -\frac{1}{V_s} \sum_{i,\bar{k},t,s,|G|>G_0} \langle \Phi_j \Phi_t|G\rangle\langle G|\Phi_s\Phi_l\rangle D^{\bar{k}*}_{si} D^{\bar{k}}_{ti} v(G). \tag{23}$$

This approximation removes the need to Fourier transform $v(r)$ for all possible combinations of $(k, \bar{k})$ per Eq. (19) in the high-G space.

The next step is the fragmented-stochastic-exchange formulation of Ref. [29],

$$\sum_G |G\rangle v(G)\langle G| = \frac{1}{N_\xi}\sum_\xi |\xi\rangle\langle\xi|, \tag{24}$$

where ξ is a fragmented-stochastic basis, here made of a set of N_ξ short random vectors in the high-G space. We define a projection $P(G)$ that randomly falls on a strip of the high-G grid, which is randomly positive or negative within the strip and zero elsewhere. Combining the projector with the Coulomb kernel yields the basis vectors, $\langle G|\xi\rangle = \pm\sqrt{\frac{N}{L}v(G)}P(G)$, where N is the length of the reciprocal-space grid being sampled and $L \sim O(N/N_\xi)$ is the length of the random vector.

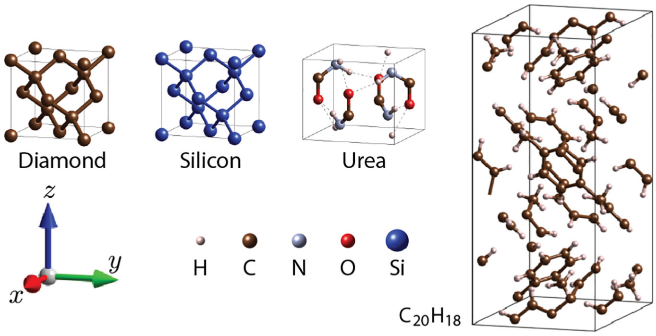

FIG. 1. Unit cells for systems studied.

The stochastic resolution of the identity above is formally exact only in the limit $N_\xi \rightarrow \infty$, but in practice, the results converge rapidly, so $N_\xi \sim 500$ is generally sufficient. Equation (24) yields

$$Y^H_{jl} \simeq -\sum_{i\bar{k}\xi} u^*_{j\xi i\bar{k}} u_{l\xi i\bar{k}}, \tag{25}$$

with

$$u_{l\xi i\bar{k}} = \sqrt{f_{i\bar{k}}}\sum_t \langle\xi|\phi_l\phi_t\rangle D^{\bar{k},*}_{ti}. \tag{26}$$

Note that Y^L scales quadratically with the number of k points, while Y^H scales only linearly. It is therefore beneficial numerically to use a lower G_0, so that only a few G vectors contribute to Y^L. We show later that the value of G_0 can be quite small, so that most G vectors can be represented stochastically with the N_ξ auxiliary basis, which does not grow with elementary cell size or number of k-points.

Equations (11)–(26) give the complete expressions for the X matrix. A technical point is that due to linear dependence considerations, the B matrix is not square; only Φ_{jk} orbitals in the small exchange-active space A are expanded, while their basis set, i.e., $\Phi_{j'}$ orbitals [Eq. (12)], encompasses the full active space M. For orbitals outside the exchange-active region, we could use a scissorslike expression,

$$X^k_{jl} = \delta_{jl}X^k_{\bar{j}\bar{j}}, \tag{27}$$

for j and l in the lower $N_v - A_v$ space, where $\bar{j}$ is the lowest orbital in the exchange-active region A, and analogously for orbitals in the $N_c - A_c$ space. An alternative would be to include the contribution of orbitals outside the A subspace stochastically [35].

III. RESULTS AND DISCUSSION

The hybrid-exchange approach presented here is benchmarked on various orthorhombic lattices, including traditional covalently bonded diamond and silicon (Si), and molecular crystals with π-π interactions: urea and 1,4-bis-(2-methylphenyl)-benzene ($C_{20}H_{18}$) [36–38]. The $C_{20}H_{18}$ unit cell consists of π-stacked layers of benzene rings arranged in a staggered geometry (see Fig. 1).

TABLE II. Band gaps (eV) for Si lattices as a function of the k-point grid size for several functionals.

k-point sampling	BNL	CL	HSE06	PBE0
$1 \times 1 \times 1$	3.73	4.87	1.77	2.50
$2 \times 2 \times 2$	3.64	4.69	1.78	2.46
$3 \times 3 \times 3$	3.88	4.58	1.84	2.57
$4 \times 4 \times 4$	3.51	4.00	1.69	2.29
$5 \times 5 \times 5$	3.79	4.18	1.74	2.48
$6 \times 6 \times 6$	3.58	3.89	1.70	2.40
$8 \times 8 \times 8$	3.61	3.78	1.73	2.44
$10 \times 10 \times 10$	3.56	3.72	1.72	2.45

LDA-DFT calculations on uniform k grids are performed using Troullier-Martins NCPPs and a kinetic-energy cutoff of 25 a.u. [39,40]. These LDA simulations provide k-dependent energies (converged to 10^{-8} a.u.) and one-electron wave functions Φ_{jk} that serve as the initial basis. To ensure basis-set convergence, the LDA-DFT calculations use at least five times more conduction than valence bands. All calculations are performed on standard 128-core AMD Rome processors. LDA simulations are parallelized over grid points, while the present method is parallelized over both grid points and wave functions.

Electronic band gaps, i.e., the difference between the conduction-band minimum (CBM) and valence-band maximum (VBM), are calculated with several hybrid functionals: the Baer-Neuhauser-Livshits (BNL) functional [15], Coulomb-attenuated method-local density approximation (CAM-LDA0) (CL) [41], HSE06, and PBE0. Table I shows the standard tabulated range-separation parameters used for CAM-LDA0 and HSE06. We use here the HSE06 value of $\gamma = 0.11$ bohr^{-1} for the BNL long-range hybrid. The choice of hybrid functional will affect the rate of band-gap convergence with respect to the number of k points. The BNL and CAM-LDA0 range-separated hybrids are long ranged and exhibit slow convergence due to the $G \simeq 0$ components of the exchange kernel. In contrast, HSE06 is short ranged and exhibits a faster rate of convergence.

We first show results for small cell-size systems, specifically Si (additional data for diamond and urea is given in the SM [32]). For small systems, the exchange-active space A includes all valence orbitals and a large number of conduction orbitals. The cutoff parameter G_0 is converged so that for all functionals, the band gaps agree within 10 meV with a fully deterministic calculation; $G_0 = 3$ a.u. is found sufficient for Si and diamond, and $G_0 = 2$ a.u. for urea. These are small values, so the number of G vectors that need to be treated exactly per Eq. (16) is only 6.1%, 1.8%, and 1.7% of the respective G spaces.

Table II shows band gaps for Si, and as is well known, for global and long-range functionals, a large number of k points is needed for convergence. Figure 2(a) shows the band structure of Si on a $10 \times 10 \times 10$ k grid with the long-range BNL XC functional. Band structures for other systems as well as comparisons to traditional nonstochastic methods [42] are provided in the SM (see also Refs. [43,44] therein) [32].

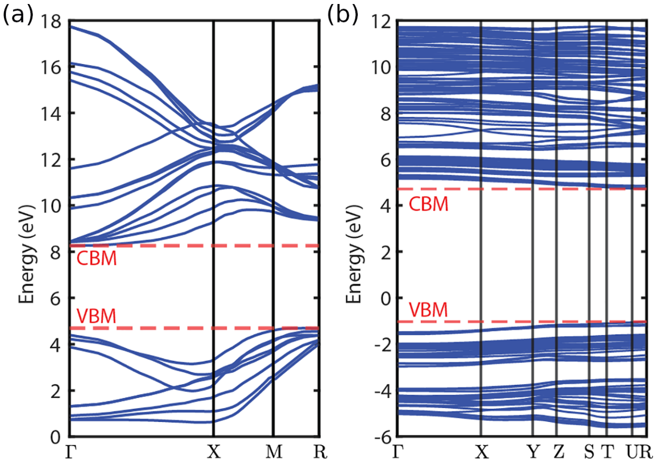

FIG. 2. Band structures of (a) Si on a $10 \times 10 \times 10$ k grid and (b) $C_{20}H_{18}$ on a $6 \times 6 \times 6$ k grid via the BNL functional. Special symmetry points are based on an orthorhombic lattice.

We next move to a larger system, $C_{20}H_{18}$, with 152 atoms within a single unit cell. Figure 1 shows the unit cell, and Figure 2(b) provides the band structure including 32 832 atoms using the BNL long-range hybrid. Table III provides band gaps for various functionals as a function of the number of k points. Due to the system's size, the molecular-orbital and exchange-active spaces are reduced to only include bands nearest to the Fermi level: $N_v = 100$, $N_c = 200$, $A_v = 50$, and $A_c = 100$. Selecting $N_v, A_v < N_{\text{occ}}$ (where N_{occ} is the number of occupied valence bands) gives an error in the band gap of roughly 200 meV; this could be remedied by a stochastic inclusion of the lower valence states, as in Ref. [35]. The results are mostly insensitive to A_c, the number of exchange-active conduction bands, as long as a sufficiently large N_c is used. Further, $G_0 = 1$ a.u. here, so only 0.2% of the G vectors are treated deterministically in the low-G space while the remaining high-G vectors are stochastically sampled with $N_\xi = 5000$ sparse-stochastic vectors.

We now move to discuss the computational cost of the new approach. Figure 3(a) shows the CPU scaling with the number of k points for urea using the PBE0 hybrid. The scaling with N_k remains quadratic for the fully deterministic calculation (blue line), while the mixed deterministic and sparse-stochastic (red line) approach scales subquadratically with a much smaller prefactor. For example, the stochastic approach requires just 1 core hour per SCF iteration for a

TABLE III. Band gaps (eV) for $C_{20}H_{18}$ (152-atom unit cell) for various functionals as a function of the number of k points.

k-point sampling	BNL	CL	HSE06	PBE0
$1 \times 1 \times 1$	6.68	7.65	4.75	5.49
$2 \times 2 \times 2$	6.31	6.90	4.37	5.04
$3 \times 3 \times 3$	6.13	6.52	4.18	4.81
$4 \times 4 \times 4$	5.91	6.38	4.15	4.75
$5 \times 5 \times 5$	5.86	6.45	4.30	4.86
$6 \times 6 \times 6$	5.74	6.32	4.22	4.78

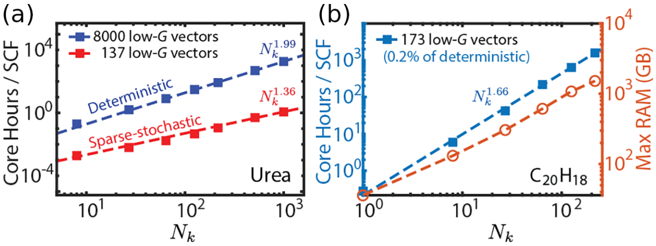

FIG. 3. CPU core hours per SCF vs number of k points (N_k) on a logarithmic scale for (a) urea and (b) $C_{20}H_{18}$. For $C_{20}H_{18}$, maximum RAM usage is shown as a function of N_k.

$10 \times 10 \times 10$ k grid, whereas a deterministic calculation demands approximately 2000 core hours per SCF.

Figure 3(b) shows the effective scaling of the method for $C_{20}H_{18}$. In addition to CPU scaling, the maximum RAM required is provided. The linear scaling of RAM requirements with the number of k points is substantially lower than a conventional PW implementation of general hybrid exchange.

Figure 4 shows the exponential convergence of the band gaps with the cubed root of the number of k points ($N_k^{1/3}$) for urea and $C_{20}H_{18}$, respectively. This allows us to extrapolate to the thermodynamic limit, i.e., $N_k \to \infty$, with modest computational resources.

The stochastic error associated with sampling the high-G exchange (i.e., Y^H) was studied for urea using the CAM-LDA0 and PBE0 hybrid functionals. With $N_\xi = 5000$, the sample standard deviation of the Γ-point band gap is small, below 10 meV. The error becomes less than 2 meV for band gaps calculated on larger k grids. The size of the sparse-stochastic basis could be reduced to even $N_\xi = 500$, as the (tiny) stochastic error stems primarily from the Monte Carlo sampling of the $G \simeq 0$ parts of the exchange kernel.

IV. CONCLUSIONS

In conclusion, we developed and benchmarked a grid-based PW implementation of GKS-DFT for periodic systems. The method scales gently with k points and provides significant speedups to deterministic calculations. This approach enables extensive k-point sampling for DFT with any hybrid-exchange functional, including long-range hybrids. The GKS-DFT energies converge with less than ten SCF iterations. This makes the present method appealing for band-structure calculations and post-DFT excited-state approaches that require GKS energies and wave functions as inputs.

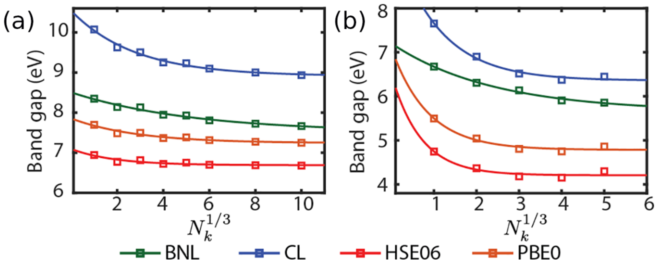

FIG. 4. Single-exponential fits of band gaps against the cubed root of the number of k points ($N_k^{1/3}$) for (a) urea and (b) $C_{20}H_{18}$.

Future work will extend the static periodic GKS-DFT formalism to linear-response time-dependent density functional theory (TD-DFT) for the optical absorption spectra of solids. In the solid state, inclusion of a long-range Coulomb tail in the exchange kernel is required to produce excitonic effects and spectra in good agreement with experiment [45,46]. In addition, this approach would be used to solve the GW-Bethe-Salpeter equation in extended systems where extensive k-point sampling is essential for accurate prediction of exciton binding energies [47].

ACKNOWLEDGMENTS

Useful discussions with Vojtech Vlcek and Laura Gagliardi are gratefully acknowledged. This work was supported by the National Science Foundation Grant No. CHE2245253. Computational resources for simulations were provided by the Expanse cluster at the San Diego Supercomputer Center through allocations CHE240067, CHE240183, PHY240131, and PHY250047, under the Advanced Cyberinfrastructure Coordination Ecosystem: Services & Support (ACCESS) program.

DATA AVAILABILITY

The data that support the findings of this article are not publicly available upon publication because it is not technically feasible and/or the cost of preparing, depositing, and hosting the data would be prohibitive within the terms of this research project. The data are available from the authors upon reasonable request.

---

[1] A. D. Becke, Density-functional thermochemistry. III. The role of exact exchange, J. Chem. Phys. **98**, 5648 (1993).

[2] A. D. Becke, A new mixing of Hartree-Fock and local density-functional theories, J. Chem. Phys. **98**, 1372 (1993).

[3] A. Seidl, A. Görling, P. Vogl, J. A. Majewski, and M. Levy, Generalized Kohn-Sham schemes and the band-gap problem, Phys. Rev. B **53**, 3764 (1996).

[4] T. Leininger, H. Stoll, H.-J. Werner, and A. Savin, Combining long-range configuration interaction with short-range density functionals, Chem. Phys. Lett. **275**, 151 (1997).

[5] B. G. Janesko, T. M. Henderson, and G. E. Scuseria, Screened hybrid density functionals for solid-state chemistry and physics, Phys. Chem. Chem. Phys. **11**, 443 (2009).

[6] S. Refaely-Abramson, S. Sharifzadeh, M. Jain, R. Baer, J. B. Neaton, and L. Kronik, Gap renormalization of molecular crystals from density-functional theory, Phys. Rev. B **88**, 081204(R) (2013).

[7] T. Stein, L. Kronik, and R. Baer, Reliable prediction of charge transfer excitations in molecular complexes using time-

dependent density functional theory, J. Am. Chem. Soc. **131**, 2818 (2009).

[8] R. Baer, E. Livshits, and U. Salzner, Tuned range-separated hybrids in density functional theory, Annu. Rev. Phys. Chem. **61**, 85 (2010).

[9] J. Heyd, G. E. Scuseria, and M. Ernzerhof, Hybrid functionals based on a screened Coulomb potential, J. Chem. Phys. **118**, 8207 (2003).

[10] J. Heyd, J. E. Peralta, G. E. Scuseria, and R. L. Martin, Energy band gaps and lattice parameters evaluated with the Heyd-Scuseria-Ernzerhof screened hybrid functional, J. Chem. Phys. **123**, 174101 (2005).

[11] F. Tran and P. Blaha, Importance of the kinetic energy density for band gap calculations in solids with density functional theory, J. Phys. Chem. A **121**, 3318 (2017).

[12] W. Chen, G. Miceli, G.-M. Rignanese, and A. Pasquarello, Nonempirical dielectric-dependent hybrid functional with range separation for semiconductors and insulators, Phys. Rev. Mater. **2**, 073803 (2018).

[13] J. P. Perdew, K. Burke, and M. Ernzerhof, Generalized gradient approximation made simple, Phys. Rev. Lett. **77**, 3865 (1996).

[14] C. Adamo and V. Barone, Toward reliable density functional methods without adjustable parameters: The PBE0 model, J. Chem. Phys. **110**, 6158 (1999).

[15] R. Baer and D. Neuhauser, Density functional theory with correct long-range asymptotic behavior, Phys. Rev. Lett. **94**, 043002 (2005).

[16] J. H. Skone, M. Govoni, and G. Galli, Self-consistent hybrid functional for condensed systems, Phys. Rev. B **89**, 195112 (2014).

[17] J. H. Skone, M. Govoni, and G. Galli, Nonempirical range-separated hybrid functionals for solids and molecules, Phys. Rev. B **93**, 235106 (2016).

[18] Z. Zheng, D. A. Egger, J.-L. Brédas, L. Kronik, and V. Coropceanu, Effect of solid-state polarization on charge-transfer excitations and transport levels at organic interfaces from a screened range-separated hybrid functional, J. Phys. Chem. Lett. **8**, 3277 (2017).

[19] S. Bhandari, M. S. Cheung, E. Geva, L. Kronik, and B. D. Dunietz, Fundamental gaps of condensed-phase organic semiconductors from single-molecule calculations using polarization-consistent optimally tuned screened range-separated hybrid functionals, J. Chem. Theory Comput. **14**, 6287 (2018).

[20] B. Joo, H. Han, and E.-G. Kim, Solvation-mediated tuning of the range-separated hybrid functional: self-sufficiency through screened exchange, J. Chem. Theory Comput. **14**, 2823 (2018).

[21] C. Chakravarty, M. A. C. Saller, H. Aksu, and B. D. Dunietz, Anisotropic dielectric screened range-separated hybrid density functional theory calculations of charge transfer states across an anthracene–TCNQ donor–acceptor interface, J. Chem. Theory Comput. **20**, 10751 (2024).

[22] L. Lin, Adaptively compressed exchange operator, J. Chem. Theory Comput. **12**, 2242 (2016).

[23] X. Wang, C. A. Lewis, and E. F. Valeev, Efficient evaluation of exact exchange for periodic systems via concentric atomic density fitting, J. Chem. Phys. **153**, 124116 (2020).

[24] K. Wu, X. Qin, W. Hu, and J. Yang, Low-rank approximations accelerated plane-wave hybrid functional calculations with *k*-point sampling, J. Chem. Theory Comput. **18**, 206 (2022).

[25] S. Sharma, A. F. White, and G. Beylkin, Fast exchange with Gaussian basis set using robust pseudospectral method, J. Chem. Theory Comput. **18**, 7306 (2022).

[26] S. Kokott, F. Merz, Y. Yao, C. Carbogno, M. Rossi, V. Havu, M. Rampp, M. Scheffler, and V. Blum, Efficient all-electron hybrid density functionals for atomistic simulations beyond 10000 atoms, J. Chem. Phys. **161**, 024112 (2024).

[27] A. Rettig, J. Lee, and M. Head-Gordon, Even faster exact exchange for solids via tensor hypercontraction, J. Chem. Theory Comput. **19**, 5773 (2023).

[28] A. Bussy and J. Hutter, Efficient periodic resolution-of-the-identity Hartree–Fock exchange method with *k*-point sampling and Gaussian basis sets, J. Chem. Phys. **160**, 064116 (2024).

[29] N. C. Bradbury, T. Allen, M. Nguyen, and D. Neuhauser, Deterministic/fragmented-stochastic exchange for large-scale hybrid DFT calculations, J. Chem. Theory Comput. **19**, 9239 (2023).

[30] M. Sereda, T. Allen, N. C. Bradbury, K. Z. Ibrahim, and D. Neuhauser, Sparse-stochastic fragmented exchange for large-scale hybrid time-dependent density functional theory calculations, J. Chem. Theory Comput. **20**, 4196 (2024).

[31] M. Rohlfing and S. G. Louie, Electron-hole excitations and optical spectra from first principles, Phys. Rev. B **62**, 4927 (2000).

[32] See Supplemental Material at http://link.aps.org/supplemental/10.1103/kr5c-csnv for convergence data, band gaps, and band structures of the diamond and urea systems, and for band structures of all systems studied in this work as well as comparisons to results obtained with the QUANTUM ESPRESSO software.

[33] S. Ismail-Beigi, Truncation of periodic image interactions for confined systems, Phys. Rev. B **73**, 233103 (2006).

[34] R. Sundararaman and T. A. Arias, Regularization of the Coulomb singularity in exact exchange by Wigner-Seitz truncated interactions: Towards chemical accuracy in nontrivial systems, Phys. Rev. B **87**, 165122 (2013).

[35] N. C. Bradbury, T. Allen, M. Nguyen, K. Z. Ibrahim, and D. Neuhauser, Optimized attenuated interaction: Enabling stochastic Bethe–Salpeter spectra for large systems, J. Chem. Phys. **158**, 154104 (2023).

[36] T. Hom, W. Kiszenik, and B. Post, Accurate lattice constants from multiple reflection measurements. II. Lattice constants of germanium silicon, and diamond, J. Appl. Crystallogr. **8**, 457 (1975).

[37] H. Guth, G. Heger, S. Klein, W. Treutmann, and C. Scheringer, Strukturverfeinerung von Harnstoff mit Neutronenbeugungsdaten bei 60, 123 und 293 K und X-N- und X-X($1s^2$)-Synthesen bei etwa 100 K, Z. Kristallogr. - Cryst. Mater. **153**, 237 (1980).

[38] L. Lunazzi, A. Mazzanti, M. Minzoni, and J. E. Anderson, Structure, conformation, and dynamic processes of the stereolabile atropisomers of hindered terphenyl hydrocarbons, Org. Lett. **7**, 1291 (2005).

[39] J. P. Perdew and Y. Wang, Accurate and simple analytic representation of the electron-gas correlation energy, Phys. Rev. B **45**, 13244 (1992).

[40] N. Troullier and J. L. Martins, Efficient pseudopotentials for plane-wave calculations, Phys. Rev. B **43**, 1993 (1991).

[41] T. Yanai, D. P. Tew, and N. C. Handy, A new hybrid exchange–correlation functional using the Coulomb-attenuating method (CAM-B3LYP), Chem. Phys. Lett. **393**, 51 (2004).

[42] P. Giannozzi, O. Baseggio, P. Bonfà, D. Brunato, R. Car, I. Carnimeo, C. Cavazzoni, S. de Gironcoli, P. Delugas, F. Ferrari Ruffino, A. Ferretti, N. Marzari, I. Timrov, A. Urru, and S. Baroni, Quantum Espresso toward the exascale, J. Chem. Phys. **152**, 154105 (2020).

[43] R. Hoffmann, How chemistry and physics meet in the solid state, Angew. Chem., Int. Ed. Engl. **26**, 846 (1987).

[44] Y. Ji, P. Lin, X. Ren, and L. He, Reproducibility of hybrid density functional calculations for equation-of-state properties and band gaps, J. Phys. Chem. A **126**, 5924 (2022).

[45] L. Reining, V. Olevano, A. Rubio, and G. Onida, Excitonic effects in solids described by time-dependent density-functional theory, Phys. Rev. Lett. **88**, 066404 (2002).

[46] G. Ohad, S. E. Gant, D. Wing, J. B. Haber, M. Camarasa-Gómez, F. Sagredo, M. R. Filip, J. B. Neaton, and L. Kronik, Optical absorption spectra of metal oxides from time-dependent density functional theory and many-body perturbation theory based on optimally-tuned hybrid functionals, Phys. Rev. Mater. **7**, 123803 (2023).

[47] A. M. Alvertis, A. Champagne, M. Del Ben, F. H. da Jornada, D. Y. Qiu, M. R. Filip, and J. B. Neaton, Importance of nonuniform Brillouin zone sampling for *ab initio* Bethe-Salpeter equation calculations of exciton binding energies in crystalline solids, Phys. Rev. B **108**, 235117 (2023).